Energy & Environmental Science

ROYAL SOCIETY OF CHEMISTRY

PAPER

View Article Online
View Journal | View Issue

Check for updates

Cite this: *Energy Environ. Sci.*, 2025, **18**, 4704

Unlocking high-performance photocapacitors for edge computing in low-light environments†

Natalie Flores-Diaz, ‡[a] Francesca De Rossi,[b] Timo Keller,[a] Harvey Morritt,[a] Zaida Perez Bassart,[cd] Amparo Lopez-Rubio, [cd] Maria Jose Fabra, [cd] Richard Freitag,[e] Alessio Gagliardi,[e] Francesca Fasulo, [f] Ana Belen Muñoz-García, [f] Michele Pavone, [g] Hamed Javanbakht Lomeri,[b] Sandy Sanchez Alonso, [h] Michael Grätzel,[h] Francesca Brunetti [b] and Marina Freitag *[a]

Received 21st February 2025,
Accepted 14th April 2025

DOI: 10.1039/d5ee01052g

rsc.li/ees

Driving continuous, low-power artificial intelligence (AI) in the Internet of Things (IoT) requires reliable energy harvesting and storage under indoor or low-light conditions, where batteries face constraints such as finite lifetimes and increased environmental impact. Here, we demonstrate an integrated three-terminal dye-sensitized photocapacitor that unites a dye-sensitized solar cell (DSC) with an asymmetric supercapacitor, leveraging molecularly engineered polyviologen electrodes and bioderived fungal-based membranes. Under 1000 lux ambient illumination, the photocapacitor delivers photocharging voltages of 920 mV, achieving power conversion efficiencies exceeding 30% and photocharging efficiencies up to 18%. Density Functional Theory calculations reveal low reorganization energies (0.1–0.2 eV) for polyviologen radical cations, promoting efficient charge transfer and stable cycling performance over 3000 charge–discharge cycles. The system reliably powers a multilayer IoT network at 500 lux for 72 hours, surpassing commercial amorphous-silicon modules by a factor of 3.5 in inference throughput. Critically, the photocapacitor driven edge microcontroller achieves 93% accuracy on CIFAR-10 classification with an energy requirement of only 0.81 mJ per inference. By eliminating the need for batteries or grid connection, this work offers a proof of concept for high-efficiency, long-lived indoor power solutions that merge advanced materials chemistry with edge AI, demonstrating a practical route toward self-sustaining, data-driven IoT devices.

Broader context

The rapid expansion of the Internet of Things (IoT) and the increasing reliance on edge-based artificial intelligence (AI) demand innovative energy solutions that are sustainable, efficient, and independent of traditional power grids. Addressing these challenges, our work introduces a groundbreaking three terminal photocapacitor that integrates a high-efficiency dye-sensitized solar cell with a polyviologen based asymmetric supercapacitor and eco-friendly fungal-based membranes. This device achieves a photo charging voltage of up to 920 mV and an overall charging efficiency of 18% under typical indoor lighting (~1000 lux), enabling battery-free operation of IoT nodes. By powering AI tasks, such as CIFAR-10 image classification with 93% accuracy at an energy cost of just 0.81 mJ per inference, our platform significantly reduces the energy overhead of data processing. Furthermore, it outperforms conventional amorphous silicon modules by 3.5 times in throughput. This innovation eliminates the need for battery replacement, paving the way for zero-maintenance, self-sustaining IoT networks. By aligning with the United Nations' Sustainable Development Goal 7, our work fosters a sustainable energy landscape for smart infrastructure, bridging the gap between energy efficiency and the growing demands of digital connectivity in smarter homes and cities.

---

[a] *School of Natural and Environmental Science, Bedson Building, Newcastle University, NE1 7RU, UK. E-mail: marina.freitag@newcastle.ac.uk*
[b] *CHOSE (Centre for Hybrid and Organic Solar Energy), Department of Electronic Engineering, University of Rome "Tor Vergata", via del Politecnico 1, 00133 Rome, Italy*
[c] *Food Safety and Preservation Department, Institute of Agrochemistry and Food Technology (IATA-CSIC), Valencia, Spain*
[d] *Interdisciplinary Platform for Sustainable Plastics Towards a Circular Economy-Spanish National Research Council (SusPlast-CSIC), Madrid, Spain*
[e] *Department of Electrical Engineering, TUM School of Computation, Information and Technology, Atomistic Modeling Center (AMC), Munich Data ScienceInstitute (MDSI), Technical University of Munich, Hans-Piloty-Straße 1, 85748 Garching, Germany*
[f] *Department of Physics "Ettore Pancini", University of Naples Federico II, Via Cintia 21, 80126 Naples, Italy*
[g] *Department of Chemical Sciences, University of Naples Federico II, Via Cintia 21, 80126 Naples, Italy*
[h] *Laboratory for Molecular Engineering of Optoelectronic Nanomaterials, Institute of Chemistry and Chemical Engineering, École Polytechnique Fédérale de Lausanne, 1015 Lausanne, Switzerland*

† Electronic supplementary information (ESI) available. See DOI: **https://doi.org/10.1039/d5ee01052g**

‡ Present address: Universidad de Costa Rica (UCR), Escuela de Ingeniería Química, San Pedro, Costa Rica.

Introduction

The exponential growth of the Internet of Things (IoT), with projections exceeding 30 billion connected devices by 2030, promises transformative advancements in areas such as smart infrastructure and personalized healthcare.[1–4] However, powering this vast network of sensors and actuators sustainably remains a critical challenge.[5,6] Ambient light harvesting, particularly in indoor environments,[7,8] offers a promising solution. However, particularly challenging is the need for efficient energy harvesting and storage in low-light conditions (100–1000 lux), where conventional photovoltaic systems struggle to maintain adequate power output and the intermittency and low intensity of indoor lighting pose significant challenges.[9–12] We address these challenges by presenting a photocapacitor (PC) design that integrates high-efficiency dye-sensitized solar cells (DSCs) with asymmetric supercapacitors (ASCs) based on engineered polyviologen materials. Recent advancements in DSCs have achieved power conversion efficiencies exceeding 38% under indoor lighting,[8] highlighting their potential for IoT applications. While other photovoltaic technologies such as perovskite, organic, and CdTe solar cells surpass 20% PCE outdoors, dye-sensitized solar cells (DSCs) achieve the highest reported efficiency under indoor lighting—reaching 38% PCE under standard office illumination (IEC TS 62607-7-2: 2023). This advantage stems from their molecular-level tunability, aligning dye absorption bands with common indoor lamp spectra. Moreover, DSCs rely on copper-based redox shuttles and stable metal oxide frameworks, eliminating hazardous materials. This is particularly critical for applications in livable and working spaces, where the use of non-toxic, environmentally safe materials is essential to ensure long-term safety. Combined with simplified manufacturing and customizable colors, DSCs are an optimal choice for integrated photocapacitors designed for continuous indoor operation. However, the intermittent nature of this energy source necessitates an integrated approach to energy storage. Photocapacitors (PCs), which combine photovoltaic (PV) energy conversion with supercapacitor-based energy storage in a single, integrated unit, offer a compelling solution.[13,14]

In PCs, the energy harvested by the PV unit can either be used directly or stored electrostatically in the supercapacitor through the electrical double layer (EDL) at the electrode–electrolyte interface.[15–17] While the concept of photocapacitors is not new,[18–22] previous implementations have struggled with low efficiency, suboptimal voltage outputs, and poor stability.[23–30] Liu *et al.* (2017) reported photocapacitors with a combined conversion and storage efficiency of 5.26% under AM 1.5G illumination,[31] while Xu *et al.* (2016) achieved a maximum photocharging voltage of 932 mV under 1 sun illumination.[32] Berestok *et al.* (2021) demonstrated photocapacitors with an overall efficiency of 11.5% under 1 sun,[33] marking notable progress but still insufficient for practical IoT applications, which typically operate in indoor environments with much lower light intensities than AM 1.5G conditions. Several recent reports have also highlighted advanced photo-rechargeable, photo-switching or photoassisted supercapacitors,[34–39] employing different photovoltaic technologies that supply energy to supercapacitor units with high specific capacitance. These studies have demonstrated the potential of integrating light harvesting with energy storage, enabling self-powered systems for diverse applications, including wearable electronics, autonomous sensors, and intermittent energy environments. Our approach builds on these breakthroughs, further optimizing edge computing applications under low-light intensities.

Although integrated photocapacitors have recently achieved light-to-charge storage efficiency of up to 21.6% (not overalll effciency),[40] further improvements in active material properties, interface quality, and device integration are necessary to enhance performance and commercial viability. The primary challenge remains in the development of materials and architectures that can efficiently harvest low-intensity light while minimizing energy losses during storage. Additionally, the demand for sustainable, non-toxic, and easily processed materials adds complexity to the design of these systems (Fig. 1a).

Our approach systematically targets these challenges by (i) exploiting DSCs for their proven low-light harvesting capabilities, (ii) introducing polyviologens materials including PV1 and the newly synthesized PVN for stable, high-capacitance energy storage, and (iii) integrating these components within a three-terminal architecture to minimize charge recombination and optimize stored voltage. This innovative photocapacitor technology is designed for efficient operation under ambient indoor lighting, achieving high photocharging voltages. By employing a three-terminal architecture, we overcome the inherent limitations of traditional two-terminal designs, reducing charge recombination and maximizing energy storage efficiency. Unlike photo-assisted supercapacitors requiring external bias or additional wiring, our three-terminal device integrates the solar cell and supercapacitor through a common PEDOT counter electrode. This unified design enables direct energy transfer from DSC to supercapacitor in real time without extra leads. This continuous charging capability aligns with the all-in-one architecture first defined by Murakami and Miyasaka.[19]

At the core of this innovation is the development of asymmetric supercapacitors (ASCs) with polyviologen materials (PV1 and PVN) as the positive electrode, a bio-based fungal-based membrane as the separator, and carbon-based negative electrodes. Viologen compounds are well-known for their efficient two-step redox reactions and exceptional thermodynamic stability, making them highly promising for long-term reliability in electrochemical energy storage. As highlighted in the comprehensive review by Bird and Kuhn,[41] and supported by subsequent studies,[42,43] polyviologens stand out due to their high capacitance, low reorganization energies (0.1–0.2 eV), and robust cycling performance. While PV1 has been previously reported, PVN is newly introduced in this work, representing a significant advancement in polyviologen-based electrode materials. Its distinctive V-shaped conformation improves ion accessibility and facilitates more efficient charge transfer, resulting in superior electrochemical performance. Compared to monomeric viologens, the polymeric forms PV1 and PVN investigated

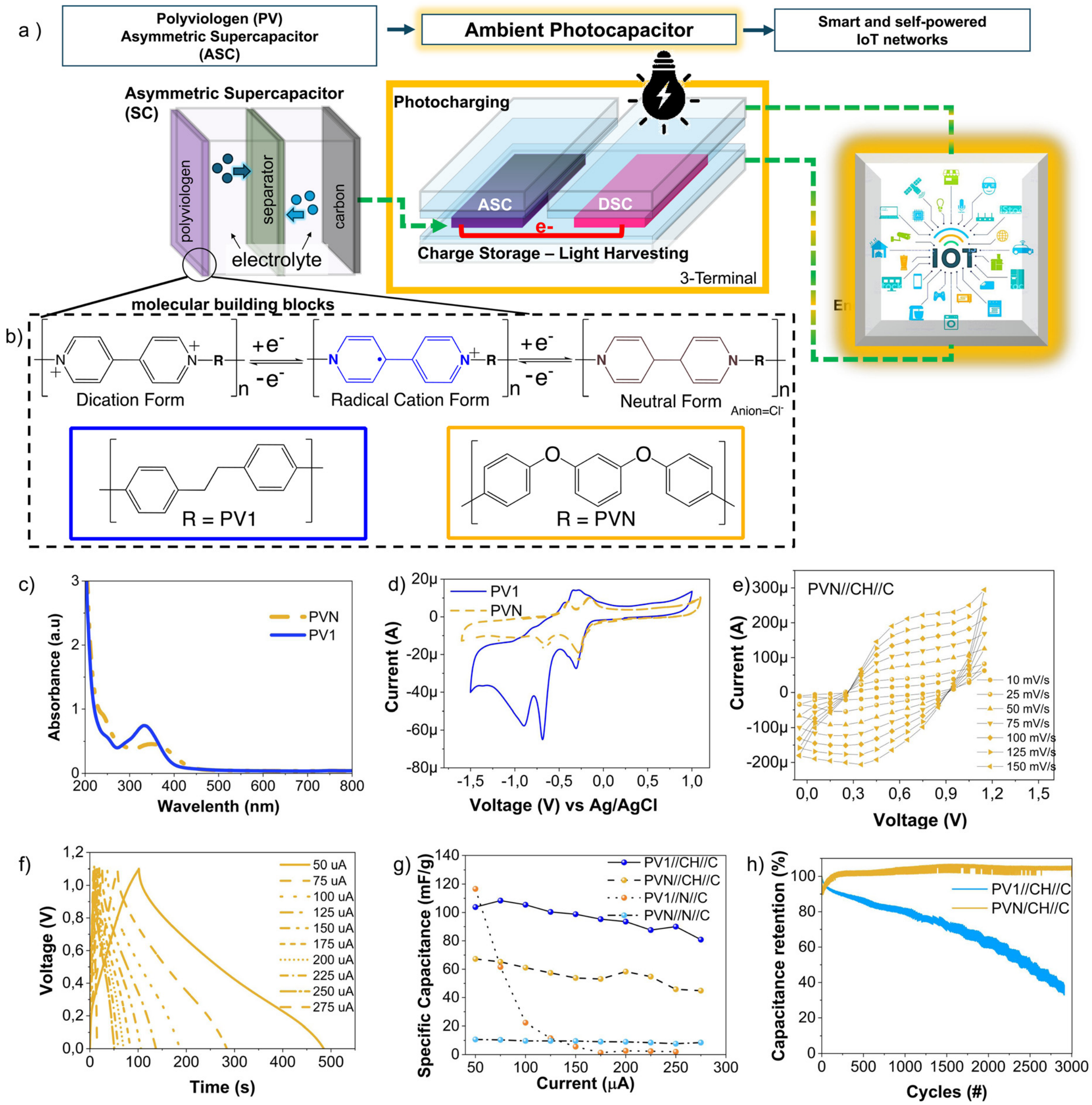

Fig. 1 (a) Ambient photocapacitor concept (b) scheme of reversible redox reaction and chemical structures of PV1 and PVN, (c) UV-vis of PV1 and PVN in MeOH, (d) CVs of PV1 and PVN in MeOH, (e) CVs of supercapacitors with PV1 and PVN and fungal-based membrane, (f) GCD measurements for supercapacitors with PV1 and PVN with fungal-based membrane (PVN//CH//C), (g) specific capacitance as a function of scan rate for supercapacitors with fungal-based and Nafion as membranes, (h) specific capacitance as a function of discharge current for supercapacitors with fungal-based and Nafion as membranes, (i) capacitance retention *vs.* cycles for the best performing supercapacitors.

here offer markedly enhanced charge storage potential. PV1 achieves specific capacitances up to 100 mF g^{-1}, while PVN demonstrates nearly 100% retention over 3000 cycles. These characteristics motivated our focus on viologen-based electrodes for photocapacitor integration, enabling rapid redox kinetics, high photovoltage tolerance, and excellent long-term electrochemical stability. Our electrochemical characterization further demonstrates that polyviologen-based ASCs achieve specific capacitance values up to 120 mF g^{-1} when coupled with fungal-based bio membranes. Through careful molecular engineering and systematic electrochemical characterization, we have tailored these materials to achieve unprecedented performance in ambient light harvesting and storage. PVN exhibits a unique V-shaped conformation, in contrast to the linear structure of PV1. This distinct structural configuration, characterized by its biphenyl-dioxy functional groups, significantly enhances ion accessibility and facilitates superior charge transfer. Density functional theory (DFT) calculations reveal that the V-shaped conformation of PVN is energetically favorable by 0.1 eV compared to its U-shaped alternative, contributing to its enhanced stability and polymerization tendency.

The optimized devices achieve photocharging voltages of up to 1.1 V under 1 sun illumination and 920 mV under 1000 lux ambient light, with power conversion efficiencies surpassing 30% and photocharging efficiencies up to 18%. This performance significantly outpaces existing technologies, setting a new benchmark for indoor energy harvesting. Furthermore, the ASCs incorporating fungal-based membranes demonstrated superior performance compared to devices with commercial Nafion membranes. The exceptional stability of the PVN-based supercapacitors is reflected in their capacitance retention, maintaining 100% of their original capacity after 3000 charge–discharge cycles. This combination of high voltage output and long-term stability makes these photocapacitors ideal for extended use in IoT applications. To demonstrate the real-world applicability of our photocapacitors, we successfully powered a wireless, battery-free, three-layer IoT network for 72 hours using only ambient light. This network implemented machine learning-based edge computing, highlighting the potential for complex data processing in energy-autonomous systems. Our PC-powered IoT system demonstrated performances approximately 3.5 times superior to that of commercial amorphous silicon modules, executing 1.90 *vs.* 0.54 predictions per hour at 1000 lux and 0.1 *vs.* 0.03 predictions per hour at 200 lux (7 *vs.* 2 predictions in 72 hours, respectively). Our work marks a significant advancement towards accomplishing the full potential of the Internet of Things, paving the way for a future where intelligent, self-powered devices seamlessly integrate into our built environment, continuously sensing, processing, and communicating data to enhance our understanding and management of the world around us.

Polyviologen supercapacitors

Viologen compounds, recognized for their reversible redox behavior and strong thermodynamic stability, offer a promising pathway for developing high-performance supercapacitor electrodes. During a redox reaction, viologens transition through three states: the oxidized form (V^{2+}), the radical cation (V^{+}) and the neutral state (V^{0}), Fig. 1b.[44] Additionally, viologens exhibit intramolecular optical charge-transfer complexation and favourable charge transfer characteristics, high capacity, fast charging, and outstanding stability.[45] These characteristics make polyviologens suitable for a wide array of technologies, including electrochromic devices, diodes, transistors, memory devices, molecular machines, supercapacitors, battery electrodes, hydrogen generation and gas storage, on-chip micro-supercapacitors (MSCs), and DSCs.[46–53]

We used the Zincke reaction to afford well-defined PV1 and PVN derivatives, controlling chain length and functional groups to optimize redox performance for integrated photocapacitors.[54,55] The synthesis of polyviologens featuring a viologen moiety and extended chains with diverse functional groups in the backbone imparts long-term stability, resulting in excellent cycle performance. Furthermore, by modifying the functional substrates, the cavity size can be controlled, leading to the formation of a porous host material.[54,55] Linear polyviologens such as PV1 (Fig. 1b), have previously been studied as anodic battery materials, demonstrating high areal and volumetric current densities when mixed with reduced graphene oxide (rGO). The resulting PV1@rGO composites showed 13.3 mA h cm^{-2} at 460 μm and 288 mA h cm^{-3} with 98% Coulombic efficiency at current densities up to 1000 A g^{-1}.[42] In this work, we introduce a novel non-linear polyviologen material, PVN, by modifying the bipyridyl core chains, and compare its performance as a supercapacitor electrode with that of the previously studied linear polyviologen material, PV1. This comparative analysis aims to highlight the unique advantages of PVN in terms of stability, charge storage, and overall electrochemical performance.

The reversible redox behaviour of viologens was confirmed through cyclic voltammetry measurements, where the compounds were deposited on fluorine-doped tin oxide (FTO) and dried before testing. For PV1, we note in Fig. 1d at −0.300 V and −0.315 V the PV^{2+}/PV^{+} reaction, while the second reaction was observed at −0.450 V and −0.670 V consistent with a quasi-reversible redox related to bipyridyl ring reductions (see Table 1). We note that the slight overlap with oxygen reduction around −0.315 V can lead to an apparent irreversibility in the blue CV curve of PV1. To confirm intrinsic reversibility, we conducted additional cyclic voltammetry at different scan rates (Fig. S7, ESI†), which yielded well-defined redox peaks with minimal peak splitting (<40 mV at 20 mV s^{-1}). Thus, the irreversibility in the original measurement is largely an artifact of unintended O_2 reduction in air-saturated solvents.

The PVN viologen (Fig. 1b) showed reversible behaviour for both oxidation/reduction processes. For both polyviologens, the first reduction step caused a transition in the color from the yellowish of PV^{2+} to the violet-blue of PV^{+}, and subsequently to the yellow-brown of PV^{0}. Cyclic voltammograms at different scan rates are provided in Fig. S7 (ESI†), where it can be observed that the oxidation and reduction peaks remain relatively constant across varying scan rates. The reversible behavior of these polyviologens indicates that high cyclability can be achieved when these materials are used in supercapacitors.

Table 1 Cyclic voltammetry parameters for the tested polyviologen materials

Polyviologen	Oxd 1 (V *vs.* Ag/AgCl)	Red 1 (V *vs.* Ag/AgCl)	E_0 1 (V *vs.* Ag/AgCl)	Oxd 2 (V *vs.* Ag/AgCl)	Red 2 (V *vs.* Ag/AgCl)	E_0 2 (V *vs.* Ag/AgCl)
PV1 solution	−0.3	−0.315	−0.3075	−0.45	−0.67	−0.56
PV1 electrode	−0.24	−0.33	−0.285	−0.71	−0.62	−0.665
PVN solution	−0.156	−0.275	−0.2155	−0.397	−0.68	−0.5385
PVN electrode	−0.129	−0.32	−0.2245	−0.393	−0.73	−0.5615

After evaluating the redox behavior of PV1 and PVN in solution, we proceeded to fabricate asymmetric supercapacitors using these polyviologens as the positive electrode material on FTO substrates. The devices featured either Nafion or fungal-based membranes and a gel-like electrolyte composed of sodium alginate, while carbon-based electrodes on FTO served as the negative electrodes. The supercapacitors were rigorously tested to assess their energy storage capabilities. The specific capacitance of the devices was calculated using eqn (2) and (1), derived from both cyclic voltammograms (CV) and galvanostatic charge–discharge (GCD) curves.

$$C = \frac{\int_a^b I(V)\mathrm{d}V}{2m\nu\Delta V} \quad (1)$$

$$C = \frac{I\Delta t}{\Delta V m} \quad (2)$$

The average specific capacitance values, derived from data across four devices for each configuration as a function of scan rate, were calculated from voltammograms (*e.g.*, Fig. 1e) using eqn (1) and are summarized in Fig. 1g. Devices with PV1//CH//C demonstrated capacitance values ranging from 50 mF g^{-1} at 10 mV s^{-1} to 35 mF g^{-1} at 150 mV s^{-1} compared to 35 mF g^{-1} at 0 mV s^{-1} to 22 mF g^{-1} at 150 mV s^{-1} for PVN//CH//C. In contrast, devices utilizing Nafion membranes exhibited substantially lower capacitance across both PV1 and PVN configurations, coupled with a pronounced initial decline in capacitance, which led to markedly shorter discharge times compared to devices with fungal-based membranes.

The GCD was evaluated at various current densities for devices employing PV1 and PVN as the positive electrodes and Nafion or fungal-based membranes (Fig. 1f). The discharge profiles from the GCD measurements are shown from Fig. S8–S11 (ESI†). The mean values of the calculated capacitance from GCD, based on data from four devices for each configuration, are summarized in Fig. S12 (ESI†), and displayed in Fig. 1h, where it can be observed that devices with fungal-based membranes exhibit longer discharge times than those with Nafion membranes for both polyviologens. Devices incorporating PV1 with fungal-based membranes demonstrated superior capacitance values compared to those using PVN, as revealed by GCD data. PV1-based supercapacitors showed capacitance values ranging from 100 mF g^{-1} at 50 μA to 85 mF g^{-1} at 275 μA, whereas PVN-based devices displayed lower values, from 67 mF g^{-1} at 50 μA to 45 mF g^{-1} at 275 μA for the PVN//CH//C configuration.

Notably, capacitance values from CV were consistently lower than those from GCD measurements. This difference arises from the distinct measurement methodologies: GCD applies a steady current, which allows a more complete assessment of the materials charge storage capacity by giving ions in the electrolyte sufficient time to diffuse and access all active sites. In contrast, CV applies a varying voltage, and at higher scan rates, the charge transfer process may be incomplete, limiting the utilization of all active sites. CV is also more prone to electrode polarization, which can further lower capacitance values by reducing the effective voltage window. Additionally, GCD captures both faradaic and non-faradaic processes more effectively than CV, particularly in systems where faradaic reactions are slower. These factors explain why GCD measurements often yield higher capacitance values compared to those obtained through CV.[56]

Comparing the performance of devices with Nafion *versus* fungal-based membranes, it is evident that replacing fungal-based with Nafion reduces capacitance for both polyviologens. The best-performing asymmetric supercapacitors, featuring PV1 and PVN as the positive electrodes, fungal-based membranes, and carbon-based negative electrodes, were subjected to long-term cycling tests. As depicted in Fig. 1i, devices with PVN electrodes exhibited exceptional performance, retaining nearly 100% of their initial capacitance after 3000 consecutive charge/discharge cycles. While PV1 exhibits higher specific capacitance (~100 mF g^{-1}) compared to PVN, it experiences a significant ~60% loss in capacity after 3000 cycles. This deterioration is evident from the cyclic voltammogram shown in Fig. 1d, where PV1 exhibits a pseudo-reversible oxidation/reduction peak along with irreversible reduction peaks, causing redox-site degradation.

This instability arises from PV1s greater structural strain during redox transitions, as indicated by its higher reorganization energy (0.35 eV *vs.* 0.2 eV for PVN) and linear conformation, which is more prone to distortion under repeated cycling In contrast, PVNs biphenyl-dioxy-bridged ''V-shaped'' structure enhances bonding stability, reduces mechanical stress, and prevents deterioration. Its lower formation energy (ΔG_f) further strengthens the polymer backbone, minimizing irreversible side reactions and chain fragmentation. These characteristics explain the stark difference observed in Fig. 1d, where PVN shows fully reversible redox peaks, while PV1 exhibits irreversible reduction features. Overall, PVNs superior charge–discharge stability makes it the preferred choice for long-term applications, while PV1 may be advantageous in scenarios prioritizing higher initial energy storage. These findings highlight the crucial role of molecular architecture in determining supercapacitor longevity and efficiency.

Electrochemical impedance spectroscopy (EIS) was performed to elucidate the fundamental properties of the polyviologens and charge transfer processes at the electrode–electrolyte interface. Nyquist plots obtained from EIS measurements at different voltages (Fig. S18, ESI†) were simulated using the equivalent circuit shown in Fig. S18a (ESI†). The extracted results from the simulations are summarized in Table 2. The internal resistance (R_{series}) is notably lower for devices utilizing Chitosan films as membranes,contributing to higher charge/discharge rates compared to those with Nafion membranes. Additionally, the charge

Table 2 EIS parameters measured at 1 V

Supercapacitor	R_{series} (Ω)	R_{CT} (Ω)	Z_{W} (Ω)	C_{EDL} (F)	C_{diff} (F)
PV1//CH//C	9.3	110.2	88.5	5.86×10^{-06}	1.53×10^{-03}
PV1//N//C	13.1	4.5	10.2	7.63×10^{-06}	7.29×10^{-04}
PVN//CH//C	9.9	68.7	54.7	4.49×10^{-06}	1.02×10^{-03}
PVN//N//C	13.5	1.5	13.4	2.07×10^{-07}	6.59×10^{-05}

transfer resistance (R_{CT}) is significantly higher for both PV1 and PVN when employing fungal-based films, suggesting reduced charge recombination rates between the electrode surface and the gel electrolyte. Interestingly, the higher RCT with fungal-based membranes suggests improved separation between electrode and electrolyte, possibly lowering recombination losses while extending discharge time. The Warburg impedance (Z_W) represents the ion diffusion in the electrolyte on the electrode interface.[57] Interestingly, the Z_W for devices with fungal-based films is higher compared to those with Nafion membranes. This increased Z_W correlates with the longer discharge times observed in the fungal-based devices, indicating that the higher impedance may facilitate a slower, more controlled ion diffusion process, ultimately extending energy release. The capacitance values obtained from the EIS data follows the same trend observed from the GCD curves in Fig. S18 (ESI†).

The electrochemical stability of PVN could be attributed to its intrinsic material properties, which better resist degradation under repeated cycling. This includes improved preservation of redox-active sites and reduced formation of detrimental byproducts, both of which contribute to sustained high capacitance over extended cycles. Additionally, the improved charge transfer dynamics observed in the EIS data suggest that PVN has superior electronic conductivity and more favorable interactions with the electrolyte, further enhancing the efficiency of charge storage and retrieval. These factors collectively explain PVN's advanced performance in maintaining long-term cycling stability.

Computational modelling of polyviologens

We investigated the structural and electronic properties of the synthesized polyviologens PV1 and PVN by means of advanced density functional theory (DFT) calculations.[58] Fig. 2a illustrates the minimum-energy structures for the monomer, dimer, and trimer derivatives of both compounds, optimized at the PBE0-D3(BJ) level of theory. While PV1 adopts a linear conformation upon dimer and trimer formation, we found two distinct conformations for PVN: a U-shaped structure (labelled PVN_U), left panel in Fig. 2(a) and a V-shaped structure (labelled PVN_V), right panel in Fig. 2(a). The computed infrared (IR) spectra for the monomer, dimer, and trimer derivatives (Fig. S28, ESI†) reveal consistent patterns for both viologens, closely resembling the experimental spectra (Fig. S28, ESI†). This strong agreement between computational and experimental IR spectra suggests a high likelihood of oligomer formation. Formation energies (ΔG_f) for the dimers and the trimers have been computed *via* the following expression:

$$\Delta G_{f,1\rightarrow2} = G_2 - 2G_1 + G_{\text{ethane}} \tag{3}$$

$$\Delta G_{f,1\rightarrow3} = G_3 - 3G_1 + 2G_{\text{ethane}} \tag{4}$$

$$\Delta G_{f,2\rightarrow3} = G_3 - G_1 - G_2 + G_{\text{ethane}} \tag{5}$$

where G_n is the free energy at PBE0-D3(BJ) level of theory of monomer (n = 1), dimer (n = 2) and trimer (n = 3), and G_{ethane} the free energy of an ethane molecule; all free energies are computed in water. The scheme from Fig. 2b presents the energetic data for these formations, providing insights into the stability of the oligomerized structures.

Both viologens exhibit slightly positive formation energies ($\sim$0.2–0.4 eV) for dimer $[PV]_2$ and trimer $[PV]_3$, which are consistent with their tendency to polymerize. For $[PV1]_2$, the dimer formation energy is about half that of the trimer ($\Delta G_{f,1\rightarrow2} \approx 0.24$ eV *vs.* $\Delta G_{f,2\rightarrow3} \approx 0.44$ eV), while for PVN, the difference between dimer$[PVN]_2$ and trimer $[PVN]_3$ formation energies is minimal (only 0.06 eV). Notably, PVN shows a preference for a more linear V-shaped conformation, with the U-shaped structure being less favorable energetically, requiring more energy for polymerization (0.76 eV for PVN_U *vs.* 0.60 eV for PVN_V). This suggests that PVN is more likely to adopt the V-shaped configuration, making it more favorable energetically compared to PV1. Further analysis on molecular orbitals (MO; Fig. S26 and S27, ESI†) reveals that the electronic structure of both viologens remains largely unchanged upon dimer and trimer formation. In all cases, the lowest unoccupied molecular orbital (LUMO) is distributed primarily on the bipyridyl groups, while the highest occupied molecular orbital (HOMO) is localized on the benzene and benzenediol rings attached to the bipyridine moiety of PV1 and PVN, respectively. As polymerization proceeds, more occupied and unoccupied states emerge, all localized similarly on the bipyridyl and benzene/benzenediol groups. These electronic transitions suggest potential intramolecular charge transfer mechanisms, aligning with observed behavior in related viologen derivatives.[48]

The absorption wavelengths were computed using time-dependent density functional theory (TD-DFT).[59] The vertical excitation energies for the electronic transitions are listed in Tables S2–S7 in the ESI.† Weak HOMO-to-LUMO transitions were observed at low energies ($\sim$450 nm) in both viologens, while higher-energy transitions align with experimental absorption wavelengths (334 nm for PV1 and 348 nm for PVN). Notably, the absorption wavelengths remain largely consistent across the monomer, dimer, and trimer forms for PV1 ($\sim$360 nm) and PVN_V ($\sim$400 nm). However, the U-shaped conformation of PVN shows lower energy bands upon trimer formation ($\sim$450 nm), further suggesting that the V-shaped conformation is more energetically favorable.

Finally, to shed light on the reductive features of the viologens we computed the internal reorganization energies (λ_r) and reductive potentials (E_r in eqn (S1), see Experimental section, ESI†). The computed λ_r and E_r are listed in Tables S2–S7 in the ESI.† Both viologens exhibit low internal reorganization energies (0.1–0.2 eV), indicating minimal structural changes upon reduction, which is favorable for efficient electron transfer processes. The reductive potentials also align well with experimental data (Table S7, ESI†), further validating our computational model. Moreover, oligomeric PV has greater reductive properties compared to monomers, suggesting that PVN, with

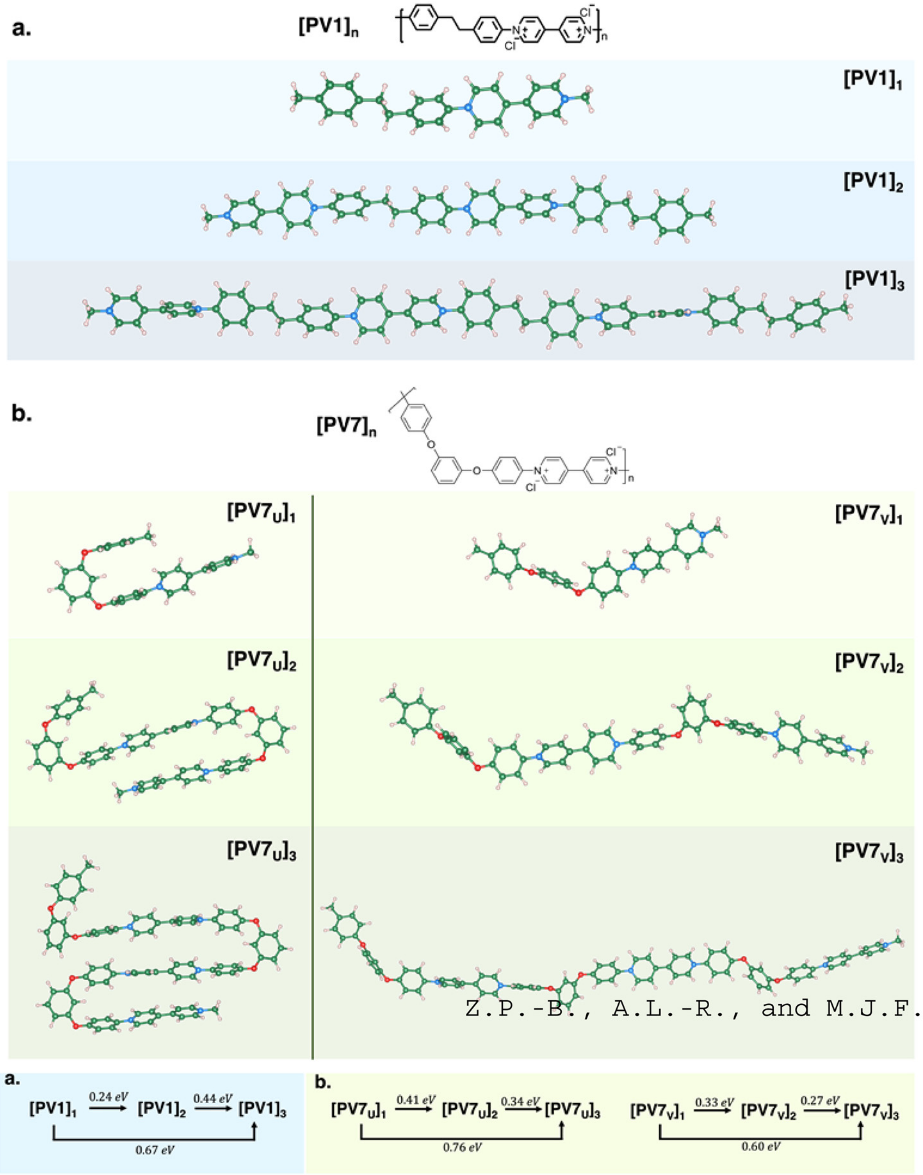

Fig. 2 (a) Minimum-energy geometries at PBE0-D3(BJ) level of theory of monomer ($[PV]_1$), dimer ($[PV]_2$) and trimer ($[PV]_3$): (top) PV1 and (bottom) PVN. Two possible conformations of PVN are considered and designated as PVN_U (left panel) and PVN_V (right panel). (b) Computed formation energies (eqn (3)–(5)) at PBE0-D3(BJ) level of theory of dimer ($[PV]_2$) and trimer ($[PV]_3$): PV1, PVN_U and PVN_V (from left to right). Color code: C (green), O (red), N (light blue), H (light pink).

its favorable polymerization tendency, has more advantageous electrochemical features.

Overall, our theoretical analysis shows that both PV1 and PVN demonstrate distinct polymerization tendencies and stable electronic properties suitable for redox applications. PVN, in particular, shows a preference for a V-shaped conformation, making it more favorable for polymerization than PV1. Thus, molecular structural differences between PV1 and PVN likely account for the observed variations in their experimental electrochemical performance, highlighting the enhanced stability and superior capacitance retention of PVN-based supercapacitors.

Photocapacitor device characterization and performance

Photocapacitors under AM 1.5G illumination

Photocapacitors under AM 1.5G illumination were studied to evaluate the impact of integrating DSCs with ASCs in a 3-T configuration. Unlike 2-terminal systems, where the recombination of extracted charges significantly reduces DSC efficiency, the 3-T architecture minimizes this issue by enabling independent control of the DSC and supercapacitor sections. This approach preserves the photovoltaic performance during charge extraction while providing better energy storage capabilities.[28]

In this study, 24 small area photocapacitors were tested under AM 1.5G conditions, incorporating a DSC of 0.32 cm^2 into a 3-Terminal architecture combined with a 0.5 cm^2 ASC for energy storage. The PC devices were characterized during both the photocharging process and subsequent constant current discharge. The potential generated by the PC was monitored by connecting a potentiostat to the ASC electrodes, allowing precise tracking of voltage evolution during charging and discharging. In this integrated configuration, the DSC unit functions as the light-harvesting component, generating photocurrent, while the polyviologen-based supercapacitor electrodes store the photogenerated charges. It is important to note that the supercapacitor itself is not photoactive. Therefore, the standard *J*–*V* curves shown in Fig. S29 (ESI†) serve as direct evidence of the system's light-harvesting capability. The *J*–*V* characteristic parameters of the DSC units are summarized in Table 3, while statistic plots are shown in Fig. S30 (ESI†). Under standard 1 sun illumination, the 24 DSC units of the photocapacitor devices (0.16 cm^2 each), measured an average V_{OC} of 0.99 ± 0.04 V (range: 0.95–1.10 V), with 1.10 V representing the upper bound of this dataset. At lower intensities (0.1 sun), the average V_{OC} was 0.91 ± 0.06 V (range: 0.85–0.95 V), where 0.95 V similarly corresponds to the upper limit. The slight variations between devices likely stem from minor differences in mesoporous TiO_2 thickness or dye loading. This aligns well with the observed distribution in Table 3. During the discharge process, the light was switched off to measure the self-discharge of the photocapacitor, without applying a negative current. As depicted in Fig. 3c–f (plots for multiple devices in Fig. S32–S34, ESI†),

Table 3 Statistics of *J*–*V* characteristic parameters from 24 photocaps with a DSC of 0.16 cm^2 active area under AM 1.5G conditions

Light intensity	V_{OC} (V)	J_{SC} (mA cm^{-2})	FF (%)	PCE (%)
1 sun	0.99 ± 0.04	14.35 ± 0.33	0.71 ± 0.01	10.08 ± 0.59
0.1 sun	0.91 ± 0.06	1.55 ± 0.03	0.77 ± 0.02	10.84 ± 0.90

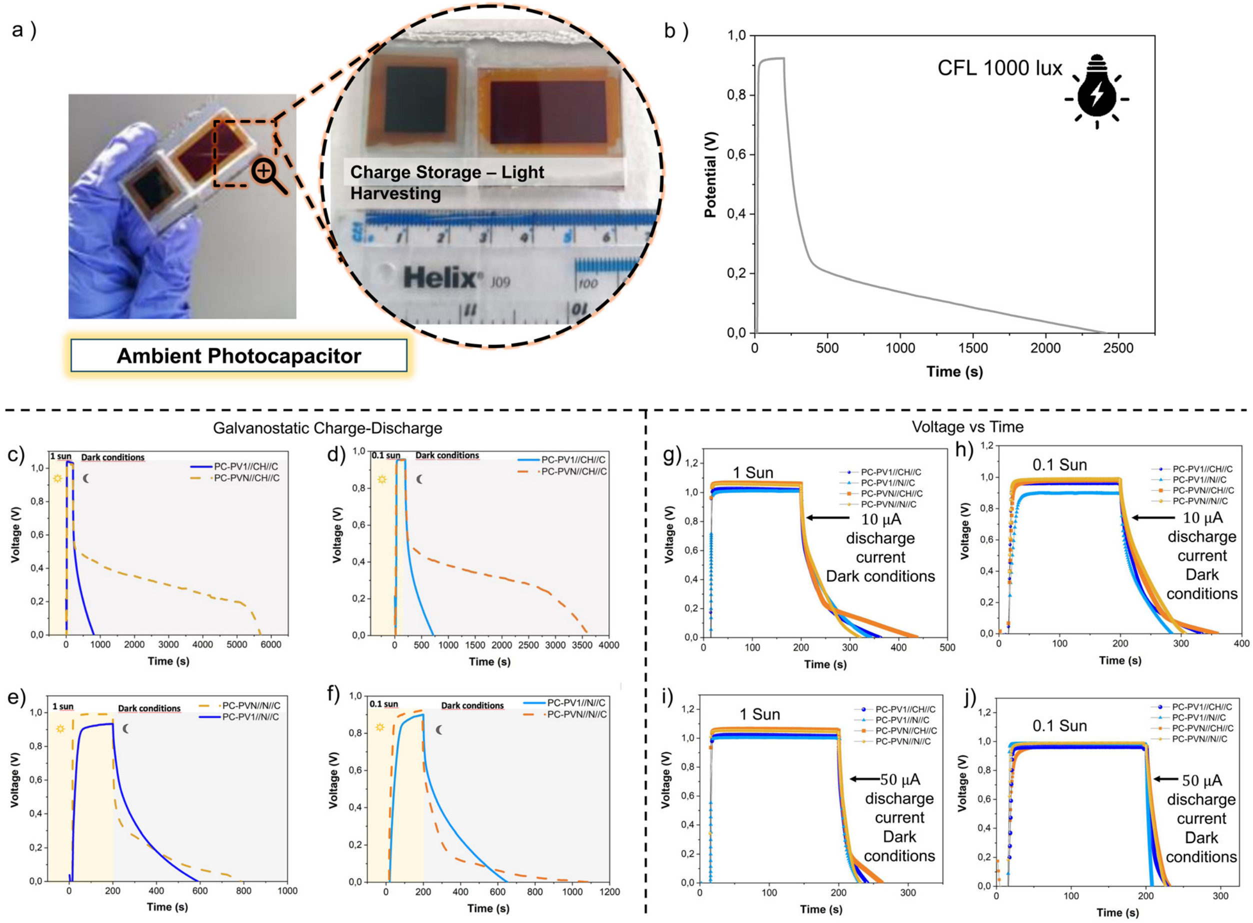

Fig. 3 (a) Schematic of the three-terminal photocapacitor architecture. The red area represents the 4.2 cm^2 light-harvesting unit (DSC), while the blue area denotes the charge storage unit (supercapacitor with PVN//CH//C). The dashed circle magnifies the complete device, highlighting its compact size and the integration of both units on a common PEDOT electrode. (b) GCD measurement at 1 μA discharge current after 3 min under 1000 lx. (c) Voltage *vs.* time for the ACS with fungal-based membranes, when the DSC is under 1 sun illumination and (d) 0.1 sun illumination. (e) Voltage *vs.* time for the ACS with Nafion membranes when the DSC is under 1 sun illumination and (f) under 0.1 sun illumination. (g) GCD measurements at 10 μA discharge current for photocapacitors irradiated at 1 sun illumination and (h) 0.1 sun illumination. (i) GCD measurements at 50 μA discharge current for photocapacitors irradiated at 1 sun illumination and (j) 0.1 sun illumination.

the PCs integrated with the polyviologen PVN and fungal-based film membranes demonstrated significantly longer self-discharge times, exceeding 5000 s under 1 sun and 3500 s under 0.1 sun illumination, reflecting their superior energy storage capability. The photocharging process was repeated with the potentiostat set to apply varying negative constant current values (discharge currents), as shown in Fig. 3g–j. Data from the galvanostatic GCD measurements of the full devices are summarized in Table 4. The photocapacitors with PVN electrodes and fungal-based membranes demonstrated the highest overall efficiencies, achieving an impressive n_{overall} of 3.53% under 1 sun and 5.82% under 0.1 sun illumination. This superior performance is attributed to the combined advantages of the polyviologen redox-active material and the fungal-based membrane's enhanced ion transport and electrolyte retention capabilities. These results underscore the potential of PVN-based 3-T photocapacitors for efficient energy storage in low-light environments, making them highly suitable for sustainable IoT and energy-harvesting applications. Although our photocapacitors are optimized for harvesting ambient light in indoor IoT applications, they also demonstrate strong performance under higher illumination. Under simulated 1 sun (AM 1.5G, 100 mW cm^{-2}) and 0.1 sun conditions, the devices achieve photocharging voltages of up to 1.1 V, with total device efficiencies (η_{overall}) reaching up to 5.82%. While DSC-only devices commonly achieve power conversion efficiencies of 10–12%, the slightly lower overall efficiencies of our devices surpass those of many state-of-the-art monolithic photo-supercapacitors. This reduction in overall efficiency reflects the inclusion of both power conversion and energy storage processes, underscoring the robust functionality and versatility of our design under both low-light and high-intensity conditions. Moreover, the ability to power IoT networks as demonstrated by our work, even with modest overall efficiencies, highlights the immense potential for future advancements. Enhancing these efficiencies could pave the way for significant breakthroughs in sustainable energy storage and self-powered electronics.

Photocapacitors under ambient light

To investigate the performance of photocapacitors under ambient light conditions, large-area devices were fabricated, focusing exclusively on the PVN polyviologen due to its superior capacitance and higher cyclability in both supercapacitors and complete photocapacitor systems. The characteristic *J*–*V* parameters of DSC with an active area of 3.8 cm^2 are summarized in Table 5 (plots for multiple devices in Fig. S37, ESI†). These large-area PCs incorporate a DSC with a 4.2 cm^2 photoactive area and a 2.3 cm^2 ASC, as depicted in Fig. 3a and Fig. S35 (ESI†). A notable observation is the substantial potential drop in these large-area PCs designed for ambient conditions (Fig. 3b and Fig. S40, ESI†), with a drop of approximately 500 mV, significantly larger than the 50 mV drop observed under 1 sun and 100 mV under 0.1 sun for smaller-area PCs. This pronounced drop can be attributed to increased charge recombination across multiple pathways in the larger hybrid device, highlighting a key limitation that must be addressed in future investigations to enhance overall efficiency of the photocapacitors. Despite this, a maximum overall efficiency of 18% was achieved under 1000 lx illumination from a CFL light source (reference spectra CIE FL10), as summarized in Table 6. This underlines the strong potential of large-area PVN-based PCs for ambient energy harvesting applications. Contrary to conventional concerns about DSC stability rooted in fully liquid electrolytes, our device leverages a quasi-solid-state 'zombie' copper-complex redox mediator, greatly reducing the risk of solvent leakage.[60] This feature extends the operational lifetime of our design under

Table 4 Characteristic parameters of full devices, illuminating the photovoltaic unit under 100 or 10 mW cm^{-2} and charging the adjacent polyviologen-based supercapacitor

Device	Power-in (mW cm^{-2})	t_{disch} (s)	t to V_{max} (s)	V_{max} (V)	IR drop (V)	C (mF g^{-1})	Energy (W h kg^{-1})	Power (W h)	n_{overall} (%)
PV1-CH-C	100	43.2	2.84	1.03	0.05	44.03	6.49	8.22	2.58
PV1-N-C	100	31.7	4.3	1.01	0.05	32.94	4.67	3.91	1.22
PVN-CH-C	100	60.9	3	1.06	0.05	60.12	9.38	11.26	3.53
PVN-N-C	100	39.4	3	1.03	0.05	40.11	5.91	7.09	2.22
PV1-CH-C	10	10.0	3	0.925	0.045	11.37	1.35	1.62	5.08
PV1-N-C	10	8.2	3.37	0.98	0.05	8.80	1.17	1.25	3.93
PVN-CH-C	10	34.4	10.11	0.982	0.102	39.00	5.22	1.86	5.82
PVN-N-C	10	44.4	28.43	0.98	0.1	50.35	6.72	0.85	2.66

Table 5 *J*–*V* characteristic parameters for 16 DSCs of 4.2 cm^2 under 1000 lx from two different ambient light sources

Source	Scan direction	Mask	V_{OC} (V)	J_{SC} (μA cm^{-2})	FF	η (%)
CFL[a]	Forward	Yes	0.89 ± 0.02	113 ± 3	0.73 ± 0.02	24.2 ± 0.9
CFL	Forward	No	0.90 ± 0.02	126 ± 5	0.73 ± 0.01	27.5 ± 1.3
CFL	Reverse	Yes	0.90 ± 0.02	113.0 ± 0.3	0.79 ± 0.01	26.7 ± 1.2
CFL	Reverse	No	0.91 ± 0.02	125 ± 5	0.80 ± 0.01	30.0 ± 1.3
LED[b]	Forward	Yes	0.89 ± 0.03	112.8 ± 1.6	0.74 ± 0.01	24.4 ± 0.7
LED	Forward	No	0.90 ± 0.02	123.9 ± 2.5	0.74 ± 0.01	27.3 ± 0.7
LED	Reverse	Yes	0.89 ± 0.03	112.7 ± 1.8	0.79 ± 0.02	26.3 ± 1.1
LED	Reverse	No	0.91 ± 0.02	123.7 ± 2.5	0.80 ± 0.01	29.7 ± 1.0

[a] CIE FL10. [b] CIE B4-LED.

Table 6 Characteristic parameters of full photocapacitor devices, illuminating the photovoltaic unit under 1.5G AM, and directing the produced charges to the adjacent polyviologen supercapacitor

Device	Power-in (mW cm^{-2})	t_{disch} (s)	t to V_{max} (s)	V_{max} (V)	IR drop (V)	C (mF g^{-1})	Energy (W h kg^{-1})	Power (W h)	$\eta_{overall}$ (%)
PVN-CH-C	0.3	2198	23	0.92	0.42	54.67	14.46	2.26	18.00

realistic indoor conditions. After 1000 hours at 1000 lux (25 °C, 50% RH), the photocapacitor retains 95% of its capacity, with the DSC maintaining 98% of its initial PCE. Under 500-hour temperature/humidity cycling (40 °C, 70% RH, alternating 12 h at 1 sun and 12 h dark), photocharging voltage retention exceeds 90%. A 72-hour continuous run in

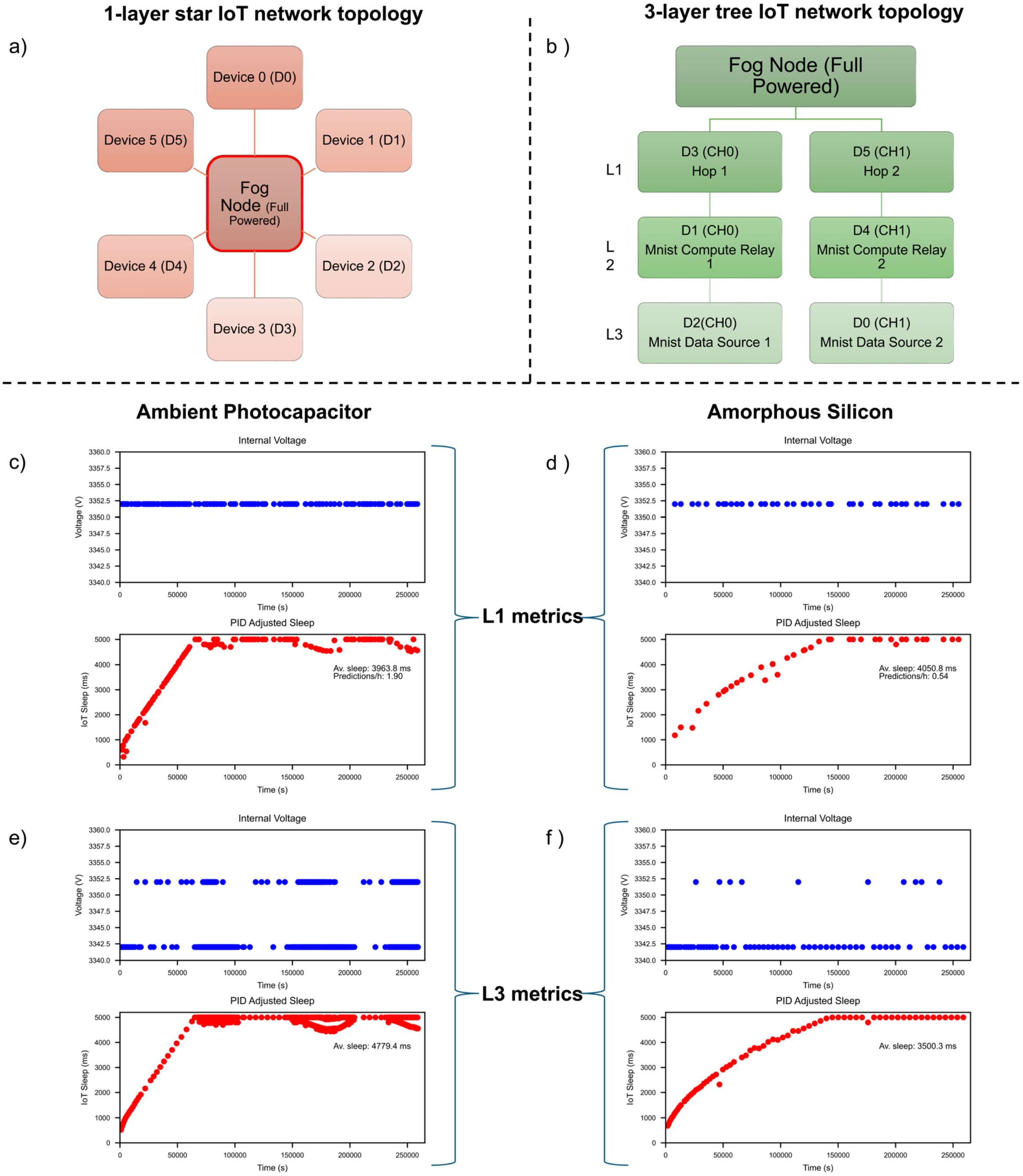

Fig. 4 IoT topologies and core performance metrics. (a) 1-Layer star IoT network for individual device performance (b) 3-layer tree topology with MNIST inference on layer 2. Layer 1 metrics for device at 1000 lx, powered by (c) ambient photocapacitor and (d) amorphous silicon. Layer 3 metrics for device powered by (e) ambient photocapacitor and (f) amorphous silicon.

Table 7 IoT device description and characterization in a single-layer IoT deployment at 1000 lx

ID/Channel	Power source	Capacitor	Packages s^{-1}	Av. sleep (ms)
2	Photocapacitor	AVX (1F)	2.940	340
1	Photocapacitor	Maxwell (1.5F)	3.889	256
3	Photocapacitor	AVX (1F)	3.364	297
0	Amorphous silicon	AVX (1F)	1.522	657
4	Amorphous silicon	Maxwell (1.5F)	1.376	726
5	Amorphous silicon	Maxwell (1.5F)	1.688	592

an IoT sensor network further confirms the stability of this quasi-solid-state DSC, ensuring long-term reliability in real-world applications.

Continuous edge computing in ambient-powered IoT networks

While battery-free IoT devices have become more ubiquitous during the last few years, including deployment in real-world applications,[61] efficient network communication remains a major challenge and research topic.[62,63] To demonstrate the practical applicability and superior performance of our high-voltage polyviologen-based photocapacitors in real-world scenarios, we developed a three-layer IoT network as outlined in Fig. 4a and b, simulating a fully autonomous IoT network, implementing control-plane and data-plane functionality on the battery-free network IoT layers 1–3, using nRF24L01+ for communication between the nodes:

- Layer 3 simulated a data-acquisition and transmission node, prepolulated with 100 MNIST images of 14 × 14 (196) bytes, sending the data to the compute node on layer 2, one 14 byte row per nRF24L01+ package.
- Layer 2 implemented a compute node, containing a pretrained network for MNIST predictions. Once a full 196 byte MNIST image was received from layer 3, an inference was calculated and the result was transmitted to the data relay on layer 1.
- Layer 1 implemented a data relay, receiving the MNIST prediction result from the layer 2 compute node, and relaying the result to the mains-powered node on layer 0 (Table 7).

Layer 0 implemented a mains-powered data-acquisition IoT controller, receiving and logging data packages from the otherwise batter-free devices on layer 1–3. Each IoT device in layer L1, L2, and L3 of the wireless IoT network implemented an adaptive intermittent sleep algorithm as multiple of 20 ms single sleep intervals, with a maximum of 250 sleep intervals (5 seconds), based on two parameters: (1) the sleep cycles of the sending node contained as a single byte in each nRF24L01+ package, and (2) a PID-controlled sleep based on the voltage of the buffer capacitor and therefore on the available harvested energy. The network was benchmarked at 1000 lx and 250 lx and the performance compared to an IoT sensor network powered by commercially available thin-film amorphous silicon flexible indoor light harvesting modules (Powerfilm LL200-4.8-3.7). The dimensions of the LL200-4.8-3.7 are 9.4 × 3.65 cm with a (measured) active area of 3.3 × 7.8 cm, thus 25.74 cm^2. The PC IoT nodes were powered by 6 PC modules with an active area of 4.2 cm^2 per PC, thus a total active area of 25.2 cm^2 (Fig. S41 and S42, ESI†). The IoT system powered by the high-voltage photocapacitors performed roughly 3.5 times better than the commercial modules, with 137 *vs.* 39 predictions at 1000 lx (1.90 predictions per hour *vs.* 0.54 predictions per hour) depicted in Fig. 4c–f and Fig. S44–S46 (ESI†), and 7 *vs.* 2 predictions at 250 lx (0.10 predictions per hour *vs.* 0.03 predictions per hour).

Conclusions

This study demonstrates significant advancements in ambient light harvesting and energy storage for wide deployment in the IoT, particularly where real-time analytics and minimal maintenance are paramount. We have developed high-performance photocapacitors that integrate DSCs with novel polyviologen-based ASCs. The three-terminal device architecture minimizes charge recombination and maximizes energy storage efficiency. These devices achieve photocharging voltages up to 920 mV under 1000 lux indoor lighting, with power conversion efficiencies exceeding 30%.

The engineered polyviologen material, PV1 and PVN, exhibits specific capacitance values up to 120 mF g^{-1} when coupled with fungal-based membranes. The reversible behavior of both viologens suggests that high cyclability can be achieved in supercapacitors incorporating these materials. This insight is crucial for optimizing the design of photocapacitors, as it implies that devices using viologen-based systems could maintain performance over extended cycles, thereby enhancing their overall efficiency and longevity. Electrochemical characterization reveals the superior performance of PVN-based ASCs, maintaining 100% capacitance retention after 3000 charge–discharge cycles. Density functional theory calculations provided insights into the electronic structure and charge transfer properties of the polyviologen materials, corroborating experimental findings. The computed low internal reorganization energies (λ_r) of 0.1–0.2 eV indicated minimal structural changes upon reduction, favorable for efficient electron transfer processes.

Real-world applicability was demonstrated by powering a three-layer IoT network implementing edge-based machine learning for 72 hours using ambient light. The system outperformed commercial amorphous silicon modules by a factor of 3.5, executing 137 *vs.* 39 predictions at 1000 lux. These results address critical challenges in IoT deployment, offering a sustainable, high-performance power source for indoor environments. The combination of high voltage output, excellent cycling stability, and ability to power complex computing tasks represents a significant step towards autonomous, maintenance-free IoT networks.

Future research should focus on optimizing polyviologen molecular structures, investigating scalable manufacturing techniques, long-term stability studies under varied environmental conditions and reducing the drop-potential in the overall device under dark cycles. This work establishes a foundation for the next generation of ambient energy harvesting technologies, potentially enabling widespread deployment of autonomous sensing networks in indoor environments.

Author contributions

N. F.-D. designed and conducted experiments, fabricated devices, performed data analysis, and co-wrote the manuscript. F. D. R. contributed to device fabrication, supercapacitor development, integration and characterization. A. G. and R. F. developed the IoT network and implemented edge computing systems. Z. P.-B., A. L.-R., and M. J. F. synthesized and characterized the fungal-based membranes. F. F., A. B. M.-G. and M. P. performed computational modeling and DFT calculations. F. F., A. B. M.-G. and M. P. assisted with theoretical analysis and data interpretation. T. K., H. M. and H. J. L. characterized and implemented polyviologen materials. S. S. A. conducted SEM imaging and film characterization. F. B. and M. F. conceived the project, supervised the research, and co-wrote the manuscript. All authors contributed to discussions and manuscript revision.

Data availability

The data supporting the findings of this study are available within the article and its ESI.† Additional raw data generated during and/or analysed during the current study are available from the corresponding author upon reasonable request. Code developed for this study, which is central to the main work described in this manuscript, is openly available on GitHub at **https://github.com/FreitagTeam/PhotoCap**. This repository contains all necessary code for reproducing the results, including scripts for data analysis, IoT network simulations, and machine learning model implementations. The authors have chosen not to use the Code Ocean platform for peer review and publication of the code. However, detailed instructions for code usage and replication of results are provided in the README file of the GitHub repository. Experimental data, including raw and processed datasets, and any additional information required to rerun the analyses, are also available in the same GitHub repository. For large datasets not suitable for GitHub storage, links to external repositories or databases are provided within the GitHub repository. Any additional data or materials that are not publicly available due to commercial or legal restrictions will be made available upon reasonable request to the corresponding author, subject to the signing of a non-disclosure or material transfer agreement.

Conflicts of interest

There are no conflicts to declare.

Acknowledgements

NFD and MF acknowledge EU Horizon 2020 MSCA-IF funding project 101028536. MF and NFD acknowledge the financial support from EPSRC UKRI for grants EP/W006340/1 and EP/V035819/1 (Photocapacitors for Ambient Energy Applications). They also thank The Royal Society for grants IES/R3/213090, RF/ERE/210025, and URF/R1/191286 (University Research Fellowships). This support has been crucial for our research in energy materials and devices. The Accreditation as Center of Excellence Severo Ochoa CEX2021-001189-S funded by MCIN/AEI/10.13039/501100011033 is also fully acknowledged by Z. P.-B., A. L.-R., and M. J. F. FB and FDR want to acknowledge the SPOT-IT project that was founded by the CETPartnership, the Clean and Energy Transition Partnership under the 2022 CETPartnership joint call for research proposal, co-founded by the European Commission (GA no. 101069750) and with the founding of the organizations detailed on **https://cetpartnership.eu/funding-agencies-and-call-moduleshttps://cetpartnership.eu/funding-agencies-and-call-modules** and the financial support of Lazio Region through the project IGEA-A0613-2023-078007.

Notes and references

1 L. Atzori, A. Iera and G. Morabito, *Comput. Networks*, 2010, **54**, 2787–2805.
2 M. Chui, M. Collins and M. Patel, *The Internet of Things: Catching up to an Accelerating Opportunity*, Mckinsey & company technical report, 2021.
3 B. N. Silva, M. Khan and K. Han, *IETE Tech. Rev.*, 2018, **35**, 205–220.
4 N. M. Karie, N. M. Sahri and P. Haskell-Dowland, *2020 Workshop Emerg. Technol. Secur. IoT ETSecIoT*, 2020, pp. 22–29.
5 E. Manavalan and K. Jayakrishna, *Comput. Ind. Eng.*, 2019, **127**, 925–953.
6 A. H. Sodhro, S. Pirbhulal, Z. Luo and V. H. C. de Albuquerque, *J. Cleaner Prod.*, 2019, **220**, 1167–1179.
7 H. Michaels, I. Benesperi and M. Freitag, *Chem. Sci.*, 2021, **12**, 5002–5015.
8 H. Michaels, M. Rinderle, I. Benesperi, R. Freitag, A. Gagliardi and M. Freitag, *Chem. Sci.*, 2023, **14**, 5350–5360.
9 I. Mathews, S. N. Kantareddy, T. Buonassisi and I. M. Peters, *Joule*, 2019, **3**, 1415–1426.
10 E. Hittinger and P. Jaramillo, *Science*, 2019, **364**, 326–328.
11 M. Freunek Müller, *Indoor Photovoltaics: Materials, Modeling and Applications*, John Wiley & Sons, Ltd, 2020, ch. 4, pp. 39–114.
12 A. H. M. E. Reinders, W. G. J. H. M. van Sark and M. Freunek Müller, *Comprehensive Renewable Energy*, Elsevier, Oxford, 2nd edn, 2022, pp. 717–742.
13 N. Flores-Diaz, F. De Rossi, A. Das, M. Deepa, F. Brunetti and M. Freitag, *Chem. Rev.*, 2023, **123**, 9327–9355.
14 C. Tuc Altaf, A. M. Rostas, A. Popa, D. Toloman, M. Stefan, N. Demirci Sankir and M. Sankir, *ACS Omega*, 2023, **8**, 47393–47411.

15 C. Huang, J. Zhang, N. P. Young, H. J. Snaith and P. S. Grant, *Sci. Rep.*, 2016, **6**, 25684.

16 R. Wang, H. Liu, Y. Zhang, K. Sun and W. Bao, *Small*, 2022, **18**, 2203014.

17 G. Z. Chen, *Int. Mater. Rev.*, 2017, **62**, 173–202.

18 T. Miyasaka and T. N. Murakami, *Appl. Phys. Lett.*, 2004, **85**, 3932–3934.

19 T. N. Murakami, N. Kawashima and T. Miyasaka, *Chem. Commun.*, 2005, 3346–3348.

20 A. P. Cohn, W. R. Erwin, K. Share, L. Oakes, A. S. Westover, R. E. Carter, R. Bardhan and C. L. Pint, *Nano Lett.*, 2015, **15**, 2727–2731.

21 M. Gong, A. Kirkeminde, N. Kumar, H. Zhao and S. Ren, *Chem. Commun.*, 2013, **49**, 9260–9262.

22 N. Bagheri, A. Aghaei, M. Y. Ghotbi, E. Marzbanrad, N. Vlachopoulos, L. Häggman, M. Wang, G. Boschloo, A. Hagfeldt, M. Skunik-Nuckowska and P. J. Kulesza, *Electrochim. Acta*, 2014, **143**, 390–397.

23 K. Gao, D. Ti and Z. Zhang, *Sustainable Energy Fuels*, 2019, **3**, 1937–1942.

24 R. Liu, C. Liu and S. Fan, *J. Mater. Chem. A*, 2017, **5**, 23078–23084.

25 W.-Y. Jin, M. M. Ovhal, H. B. Lee, B. Tyagi and J.-W. Kang, *Adv. Energy Mater.*, 2021, **11**, 2003509.

26 S. B. Srivastava, R. Melikov, E. Yildiz, U. M. Dikbas, S. Sadeghi, I. H. Kavakli, A. Sahin and S. Nizamoglu, *J. Mater. Chem. C*, 2021, **9**, 1755–1763.

27 Y. Jin, Z. Li, L. Qin, X. Liu, L. Mao, Y. Wang, F. Qin, Y. Liu, Y. Zhou and F. Zhang, *Adv. Mater. Interfaces*, 2017, **4**, 1700704.

28 A. Scalia, F. Bella, A. Lamberti, C. Gerbaldi and E. Tresso, *Energy*, 2019, **166**, 789–795.

29 M. Yilmaz, S.-H. Hsu, S. Raina, M. Howell and W. P. Kang, *J. Renewable Sustainable Energy*, 2018, **10**, 063503.

30 Q. J. Yeow, C. Cuhadar, W. K. Tay, E. L. J. Tan, K. Johnson, S. E. Whang and H. N. Tsao, *ACS Appl. Energy Mater.*, 2022, **5**, 6746–6753.

31 Z. Liu, Y. Zhong, B. Sun, X. Liu, J. Han, T. Shi, Z. Tang and G. Liao, *ACS Appl. Mater. Interfaces*, 2017, **9**, 22361–22368.

32 J. Xu, Z. Ku, Y. Zhang, D. Chao and H. J. Fan, *Adv. Mater. Technol.*, 2016, **1**, 1600074.

33 T. Berestok, C. Diestel, N. Ortlieb, J. Buettner, J. Matthews, P. S. C. Schulze, J. C. Goldschmidt, S. W. Glunz and A. Fischer, *Sol. RRL*, 2021, **5**, 2100662.

34 U. Basak, P. Ghosh, D. P. Chatterjee, G. Mahapatra, A. Banerjee and A. K. Nandi, *J. Mater. Chem. A*, 2025, **13**, 7813–7833.

35 W. S. Cho, J. Y. Park, W. J. Dong and J.-L. Lee, *ACS Appl. Mater. Interfaces*, 2024, **16**, 39232–39240.

36 Y. Zhao, H. Li, R. Tang, X. Wang, Y. Wu, S. Yan and Y. Zhang, *J. Mater. Chem. A*, 2023, **11**, 15844–15854.

37 T. Zhu, J. Pan, Z. An, R. Zhe, Q. Ou and H. E. Wang, *J. Mater. Chem. A*, 2022, **10**, 20375–20385.

38 T. Zhu, Z. He, Z. An, R. Xu, Y. Li, R. Zhe, H. E. Wang and H. Pang, *Sci. China: Mater.*, 2023, **66**, 2216–2226.

39 Y. Ren, T. Zhu, Y. Liu, Q. Liu and Q. Yan, *Small*, 2021, **17**, 2008047.

40 Md Aftabuzzaman, Masud, H. Zhou, H. M. Kim, Y. Kang and H. K. Kim, *Small*, 2024, **20**, 2302826.

41 C. L. Bird and A. T. Kuhn, *Chem. Soc. Rev.*, 1981, **10**, 49–82.

42 S. M. Beladi-Mousavi, S. Sadaf, A. M. Mahmood and L. Walder, *ACS Nano*, 2017, **11**, 8730–8740.

43 K. Madasamy, D. Velayutham, V. Suryanarayanan, M. Kathiresan and K.-C. Ho, *J. Mater. Chem. C*, 2019, **7**, 4622–4637.

44 L. Striepe and T. Baumgartner, *Chem. – Eur. J.*, 2017, **23**, 16924–16940.

45 L. Cao, S. Sadaf, S. M. Beladi-Mousavi and L. Walder, *Eur. Polym. J.*, 2013, **49**, 1923–1934.

46 J. Ding, C. Zheng, L. Wang, C. Lu, B. Zhang, Y. Chen, M. Li, G. Zhai and X. Zhuang, *J. Mater. Chem. A*, 2019, **7**, 23337–23360.

47 L. Wang, J. Ding, S. Sun, B. Zhang, X. Tian, J. Zhu, S. Song, B. Liu, X. Zhuang and Y. Chen, *Adv. Mater. Interfaces*, 2018, **5**, 1701679.

48 Y. Zhuang, W. Zhao, L. Wang, F. Li, W. Wang, S. Liu, W. Huang and Q. Zhao, *Sci. China: Chem.*, 2020, **63**, 1632–1644.

49 M. Porel, A. Klimczak, M. Freitag, E. Galoppini and V. Ramamurthy, *Langmuir*, 2012, **28**, 3355–3359.

50 M. Freitag and E. Galoppini, *Langmuir*, 2010, **26**, 8262–8269.

51 S. Sen, J. Saraidaridis, S. Y. Kim and G. T. R. Palmore, *ACS Appl. Mater. Interfaces*, 2013, **5**, 7825–7830.

52 Y. Alesanco, A. Viñuales, G. Cabañero, J. Rodriguez and R. Tena-Zaera, *ACS Appl. Mater. Interfaces*, 2016, **8**, 29619–29627.

53 M. Lee, U. H. Choi, R. H. Colby and H. W. Gibson, *Macromol. Chem. Phys.*, 2015, **216**, 344–349.

54 N. Wang, A. Kähkönen, P. Damlin, T. Ääritalo, J. Kankare and C. Kvarnström, *Electrochim. Acta*, 2015, **154**, 361–369.

55 K. Madasamy, D. Velayutham, V. Suryanarayanan, M. Kathiresan and K.-C. Ho, *J. Mater. Chem. C*, 2019, **7**, 4622–4637.

56 Y. Ge, X. Xie, J. Roscher, R. Holze and Q. Qu, *J. Solid State Electrochem.*, 2020, **24**, 3215–3230.

57 J. Huang, *Electrochim. Acta*, 2018, **281**, 170–188.

58 W. Koch and M. C. Holthausen, *A Chemist's Guide to Density Functional Theory*, John Wiley & Sons, Ltd, 2nd edn, 2001.

59 C. Ullrich, *Time-Dependent Density-Functional Theory: Concepts and Applications*, Oxford University Press, Oxford, 2011.

60 M. Freitag, Q. Daniel, M. Pazoki, K. Sveinbjörnsson, J. Zhang, L. Sun, A. Hagfeldt and G. Boschloo, *Energy Environ. Sci.*, 2015, **8**, 2634–2637.

61 M. Afanasov, N. A. Bhatti, D. Campagna, G. Caslini, F. M. Centonze, K. Dolui, A. Maioli, E. Barone, M. H. Alizai, J. H. Siddiqui and L. Mottola, *Proc. 18th Conf. Embed. Networked Sens. Syst.*, New York, NY, USA, 2020, pp. 368–381.

62 K. Geissdoerfer, M. Chwalisz and M. Zimmerling, *Proc. 17th Conf. Embed. Networked Sens. Syst.*, New York, NY, USA, 2019, pp. 83–95.

63 K. Geissdoerfer and M. Zimmerling, *19th USENIX Symposium on Networked Systems Design and Implementation (NSDI 22)*, 2022, pp. 419–435.